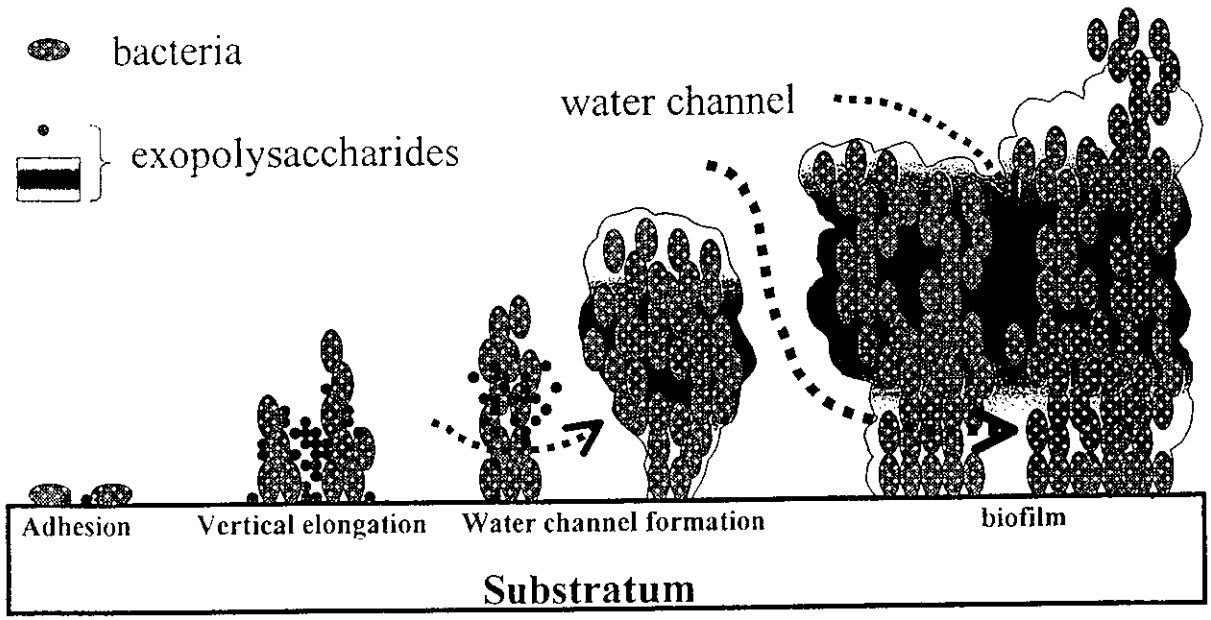

Figure 9. Scheme of time-dependent formation of biofilm architecture.

necessary in electron microscopy. In the early phase [3 h after plating: Figs. 1 and 2(A)], *E. coli* YMel emitting green fluorescence spottily aggregated on the PU surface and then vertically elongated. The number of aggregates increased with incubation time and scattered EPS-rich domains were observed [Figs. 1 and 2(A)]. Finally, a 3D structure including water channels was formed. The thickness of the biofilm increased with time, reaching to several tens of microns at 24 h after plating [Fig. 2(B)]. The channels as integral parts of the biofilm structure, which were identified as a black spotty area at 12 and 24 h of incubations (Fig. 1), are, in essence, the lifeline of the system, because they provide a means of circulating nutrients as well as exchanging metabolic products such as oxygen.[10] Interestingly, a dense interpenetrable structure of biofilm composed of *E. coli* and EPS, which was observed as the yellow region in Figures 1 and 2, existed at the middle part of the thick biofilm. Such time-dependent morphological events including bacterial adhesion, the secretion and organization of EPS, colony formation, and biofilm formation with water channels are shown in Figure 9.

As for the quantification of *E. coli* cells in biofilms, the fluorescence intensity of GFP expressed by adhered *E. coli* cells, which is directly proportional to the viable-bacterial count obtained by the plate count method (Fig. 5), allows us to easily and rapidly determine the number of adhered *E. coli* cells as compared with the conventional plate count method which requires overnight culture to detect colony formation. The growth rate of the *E. coli* cells examined for up to 24 h showed that the number of adhered and proliferated *E. coli* cells increased exponentially with time up to 12 h, and then appeared to increase at a markedly reduced rate with prolonged time, regardless of the initial bacterial cell concentration.

Many studies have reported that bacterial adhesion to and biofilm formation on material surfaces are affected by the type of protein adsorbed to the surfaces.[19-22] In the present study, three kinds of protein were preadsorbed: fibronectin and vitronectin as cell-adhesive proteins, and albumin as a non-cell-adhesive protein. Regardless of the presence or absence and the type of preadsorbed protein, there was only a small difference in the number of bacterial adhesion up to 12 h. Among the proteins tested, only fibronectin exhibited a markedly high proliferation activity only at 24 h of incubation, whereas albumin exhibited a high inhibitory activity against bacterial proliferation at 24 h of incubation. There is a small difference in bacterial proliferation activity between the vitronectin-coated and noncoated PU surfaces. This may be because the *E. coli* YMel does not produce curli in the early phase for up to 12 h of incubation but produces abundant curli (Fig. 4) in the biofilm at 24 h of incubation, although YMel does not produce curli in the planktonic state at 37°C.[23] These results are consistent with the finding by Kikuchi et al:[24] that curli were expressed in biofilm after growth at 37°C. Because curli specifically bind to fibronectin and are associated with biofilm maturation, curli-mediated biofilm formation occurred on the fibronectin-coated PU surface with a prolonged incubation time. However, the curli-deficient isogenic mutant, YMel-1, did not enhance bacterial adhesion and proliferation on the fibronectin-coated PU surface (Fig. 8).

In conclusion, we developed a novel method of deter-

mining morphological events during biofilm formation on synthetic polymers using GFP-expressing *E. coli* under CLSM observation, without the destruction of very fragile 3D structures, which may help logical surface design with a high antibacterial potential.

The authors thank T. Kikuchi, K. Yasutake, E. Koga, and M. Sato for technical assistance, and T. Kanemaru and A. Takade for electron microscopic examination.

References

1. An YH, Friedman RJ. Concise review of mechanisms of bacterial adhesion to biomaterial surfaces. J Biomed Mater Res 1998;43:338–348.
2. Gristina AG. Biomaterial-centered infection: microbial adhesion versus tissue integration. Science 1987;237:1588–1595.
3. Davies D. Understanding biofilm resistance to antibacterial agents. Nat Rev Drug Discov 2003;2:114–122.
4. Sung JY, Leung JW, Shaffer EA, Lam K, Costerton JW. Bacterial biofilm, brown pigment stone and blockage of biliary stents. J Gastroenterol Hepatol 1993;8:28–34.
5. Bryers JD, Hendricks S. Bacterial infection of biomaterials. Ann NY Acad Sci 1997;31:127–137.
6. Higashi JM, Wang IW, Shlaes DM, Anderson JM, Marchant RE. Adhesion of *Staphylococcus epidermidis* and transposon mutant strains to hydrophobic polyethylene. J Biomed Mater Res 1998; 39:341–350.
7. Merritt K, Gaind A, Anderson JM. Detection of bacterial adherence on biomedical polymers. J Biomed Mater Res 1998;39: 415–422.
8. Speer AG, Cotton PB, Rode J, Seddon AM, Neal CR, Holton J, Costerton JW. Biliary stent blockage with bacterial biofilm. A light and electron microscopy study. Ann Intern Med 1988;108: 546–553.
9. van Berkel AM, van Marle J, van Veen H, Groen AK, Huibregtse K. A scanning electron microscopic study of biliary stent materials. Gastrointest Endosc 2000;51:19–22.
10. Davey ME, O'toole GA. Microbial biofilms: from ecology to molecular genetics. Microbiol Mol Biol Rev 2000;64:847–867.
11. Cowan SE, Gilbert E, Khlebnikov A, Keasling JD. Dual labeling with green fluorescent proteins for confocal microscopy. Appl Environ Microbiol 2000;66:413–418.
12. Decho AW, Kawaguchi T. Confocal imaging of *in situ* natural microbial communities and their extracellular polymeric secretions using Nanoplast resin. Biotechniques 1999; 27:1246–1252.
13. Strathmann M, Wingender J, Flemming HC. Application of fluorescently labelled lectins for the visualization and biochemical characterization of polysaccharides in biofilms of *Pseudomonas aeruginosa*. J Microbiol Methods 2002;50:237–248.
14. Olsen A, Wick MJ, Morgelin M, Bjorck L. Curli, fibrous surface proteins of *Escherichia coli*, interact with major histocompatibility complex class I molecules. Infect Immun 1998;66:944–949.
15. Prigent Combaret C, Prensier G, Le Thi TT, Vidal O, Lejeune P, Dorel C. Developmental pathway for biofilm formation in curli-producing *Escherichia coli* strains: role of flagella, curli and colanic acid. Environ Microbiol 2000;2:450–464.
16. Olsen A, Jonsson A, Normark S. Fibronectin binding mediated by a novel class of surface organelles on *Escherichia coli*. Nature 1989;338:652–655.
17. Andersen JB, Sternberg C, Poulsen LK, Bjorn SP, Givskov M, Molin S. New unstable variants of green fluorescent protein for studies of transient gene expression in bacteria. Appl Environ Microbiol 1998;64:2240–2246.
18. Danese PN, Pratt LA, Kolter R. Exopolysaccharide production is required for development of *Escherichia coli* K-12 biofilm architecture. J Bacteriol 2000;182:3593–3596.
19. Froman G, Switalski LM, Faris A, Wadstrom T, Hook M. Binding of *Escherichia coli* to fibronectin. A mechanism of tissue adherence. J Biol Chem 1984;259:14899–14905.
20. Yu JL, Ljungh A, Andersson R, Jakab E, Bengmark S, Wadstrom T. Promotion of *Escherichia coli* adherence to rubber slices by adsorbed fibronectin. J Med Microbiol 1994;41:133–138.
21. Yu JL, Andersson R, Wang LQ, Bengmark S, Ljungh A. Fibronectin on the surface of biliary drain materials: a role in bacterial adherence. J Surg Res 1995;59:596–600.
22. Yu JL, Andersson R, Ljungh A. Protein adsorption and bacterial adhesion to biliary stent materials. J Surg Res 1996;62:69–73.
23. Bian Z, Brauner A, Li Y, Normark S. Expression of and cytokine activation by *Escherichia coli* curli fibers in human sepsis. J Infect Dis 2000;181:602–612.
24. Kikuchi T, Mizunoe Y, Takade A, Yoshida S. Curli is required for development of biofilm architecture in *Escherichia coli* K-12 and enhance bacterial adherence to human uroepithelial cells. In preparation.

Photocurable Biodegradable Liquid Copolymers: Synthesis of Acrylate-End-Capped Trimethylene Carbonate-Based Prepolymers, Photocuring, and Hydrolysis

Takehisa Matsuda, Il Keun Kwon, and Satoru Kidoaki

Division of Biomedical Engineering, Graduate School of Medicine, Kyushu University, 3-1-1 Maidashi, Higashi-ku, Fukuoka 812-8582, Japan

BioMACROMOLECULES

Reprinted from
Volume 5, Number 2, Pages 295–305

Photocurable Biodegradable Liquid Copolymers: Synthesis of Acrylate-End-Capped Trimethylene Carbonate-Based Prepolymers, Photocuring, and Hydrolysis

Takehisa Matsuda,* Il Keun Kwon, and Satoru Kidoaki

Division of Biomedical Engineering, Graduate School of Medicine, Kyushu University, 3-1-1 Maidashi, Higashi-ku, Fukuoka 812-8582, Japan

Received July 9, 2003; Revised Manuscript Received October 10, 2003

Various photocurable liquid biodegradable trimethylene carbonate (TMC)-based (co)oligomers were prepared by ring-opening (co)polymerization of TMC with or without L-lactide (LL) using low molecular weight poly(ethylene glycol) (PEG) (mol wt 200, 600, or 1000) or trimethylolpropane (TMP) as an initiator. Resultant (co)oligomers were pastes, viscous liquids, or liquids at room temperature, depending on the monomer composition and monomer/initiator ratio. Liquid (co)oligomers were subsequently end-capped with acrylate groups. Upon visible-light irradiation in the presence of camphorquinone as a radical generator, rapid liquid-to-solid transformation occurred to produce photocured solid. The photocuring yield increased with photoirradiation time, photointensity, and camphorquinone concentration. The photocured polymers derived from low molecular weight PEG (PEG200) and TMP exhibited much reduced hydrolysis potential compared with PEG1000-derived polymers in terms of weight loss, water uptake, and swelling depth. Force−distance curve measurements by nanoindentation using atomic force microscopy clearly showed that Young's moduli of the photocured polymer films decreased with increasing hydrolysis time. Their potential biomedical applications are discussed.

Introduction

Biodegradable polymers such as high molecular weight polyesters have been widely used in biomedical applications including structural supports such as sutures or bone pins, matrixes for controlled release of drugs, and scaffolds for tissue-engineered devices.[1−6] On the other hand, less attention has been paid to liquid photocurable low molecular weight (co)oligomers or prepolymers. If a biodegradable liquid prepolymer can be rapidly transformed into a solid by photoirradiation with visible or ultraviolet light in the presence of an appropriate photoinduced radical generator, such versatility may provide additional benefits in medical applications. The advantages of photopolymerization over other chemical or physical cross-linking techniques are (1) rapid curing that proceeds at room temperature and (2) in situ spatial and temporal control of the polymerization. These allow development of injectable gelable mold and in situ gelable drug-releasing matrix,[7,8] and precision fabrication including macroshaping of a device, surface microarchitecturing, and scaffold design for engineered tissues and artificial implants.[9,10]

The preparation of biodegradable liquid polymers is limited within a certain range of compositions and molar ratios of (co)polyesters. Conventional polyesters such as poly(glycolic acid) (PGA), poly(L-lactic acid) (PLLA), and poly(ϵ-caprolactone) (PCL) are crystallizable solids with a high glass transition temperatures (T_g). On the other hand, aliphatic poly(carbonate)s have relatively low T_g and are amorphous in nature. Poly(trimethylene carbonate) (PTMC), which has a low T_g (−38 to −17 °C) that depends on the molecular weight, is amorphous and exhibits an extremely slow degradation rate in water compared with polyesters.[11−13] The oligomer of TMC and its co-oligomer with CL are liquids.[14−19] Our previous studies showed that such co-oligomers end-capped with photoreactive groups such as coumarin,[14−17] phenyl azide,[18] or acrylate[19] were rapidly converted to solids upon photoirradiation. Their photocuring characteristics and hydrolytic behavior were studied in detail. In addition, stereolithographic microarchitectures were demonstrated using a custom-designed automated mobile photoirradiation apparatus.[9]

In this paper, as part of a series of our studies on biodegradable liquid photocurable prepolymers, we prepared liquid photocurable oligomers of TMC and co-oligomers with LL using low molecular weight poly(ethylene glycol) (PEG) or trimethylolpropane (TMP) as an initiator, followed by acrylation at terminal ends. Acrylate-end-capped liquid prepolymers were subjected to photocuring by visible-light irradiation. The dependence of photocuring characteristics on material properties and irradiation conditions was first described, followed by detailed analysis of hydrolytic behavior including surface erosion characteristics using confocal laser scanning microscopy (CLSM) to determine the depth profile of the water-swellable layer and using atomic force microscopy (AFM) to determine the mechanical

* To whom correspondence should be addressed. E-mail: matsuda@med.kyushu-u.ac.jp. Tel: +81-92-642-6210. Fax: +81-92-642-6212.

10.1021/bm034231k CCC: $27.50
Published on Web 12/12/2003

properties of the nanoscale water-swellable layer. Potential biomedical applications are discussed.

Experimental Section

General Procedure. All solvents and reagents were purchased from either Wako Pure Chemical Industries, Ltd. (Osaka, Japan) or Sigma-Aldrich Japan, Inc. (Tokyo, Japan). Trimethylene carbonate (TMC) was prepared according to the method described in our previous paper and recrystallized from a mixed solvent of ethyl acetate and hexane.[15] Trimethylolpropane (TMP) and L-lactide (LL) were recrystallized from acetone and ethyl acetate, respectively. Poly(ethylene glycol) (PEG) was purified by precipitation from cold hexane and subsequently dried under vacuum prior to use. Acryloyl chloride and camphorquinone were used as received without further purification. Other solvents and reagents were purified by distillation. ^{1}H NMR spectra were recorded on a JNM-AL300 (JEOL, Tokyo, Japan). Chemical shifts are given in δ values from Me_4Si as an internal standard. The number-average molecular weight (M_n) of each polymer was determined by gel permeation chromatography (GPC), which was carried out on a high-performance liquid chromatograph (HPLC, JASCO-JMBS, Tokyo, Japan) equipped with a TSK-GEL column α-3000 (TOSOH, Tokyo, Japan) using PEG as a standard and tetrahydrofuran (THF) as a solvent. Visible-light irradiation was carried out using a TOKUSO Power Lite (xenon lamp with UV and IR cutoff filter, Tokyo, Japan), and irradiation intensity was measured with a photometer (Laser power meter HP-1: Pneum Co., Ltd., Saitama, Japan) at 488 nm.

Synthesis of (Co)Oligomer. A typical procedure for the preparation was as follows. A reaction mixture of 0.33 M tin(II) 2-ethylhexanoate solution in toluene (35 μL, 12 μmol) as a catalyst, PEG (mol wt 1000, 7.6 g, 7.6 mmol), and TMC (10.21 g, 100 mmol) was stirred for 4 h at 200 °C, followed by heating for 2 h at 160 °C in a 100 mL round-bottom flask under a N_2 atmosphere. Then the solution was cooled, dissolved in dichloromethane, and added dropwise into an excess of hexane. Upon decantation of the hexane, the precipitated viscous liquid was redissolved in dichloromethane and again precipitated from excess hexane. After hexane was removed by vacuum-drying at 50 °C for 1 day, a viscous liquid at room temperature was obtained. Analysis of this liquid showed the following results: yield = 16.9 g (95%); $M_n = 2.24 \times 10^3$ (eluent, THF); ^{1}H NMR (300 MHz, $CDCl_3$, ppm) δ = 2.06 (multiplet), 3.65 (triplet), and 4.24 (multiplet).

Synthesis of Acrylate-End-Capped Prepolymer. A representative procedure for acrylation of terminal ends of the oligomers is as follows. The prepolymer (16.5 g) was dissolved in 100 mL of dichloromethane in a 200 mL round-bottom flask cooled to 0 °C. Acryloyl chloride (6 mL) was added to this flask under N_2 atmosphere and the reaction mixture was stirred for 8 h at 50 °C. The prepolymer was precipitated from excess hexane and dried at 30 °C under vacuum for 1 day. The yield was 16.8 g (94%). The acrylate content was determined from the relative peak intensities in the ^{1}H NMR spectra between the vinyl group and PEG or TMP unit yielding the following results: ^{1}H NMR (300 MHz, $CDCl_3$, ppm) δ = 2.05 (multiplet), 3.65 (doublet), 4.24 (multiplet), 5.85 (doublet), 6.12 (quartet), and 6.42 (doublet).

Visible-Light-Induced Photocuring. Camphorquinone-containing dichoromethane solution (20 wt %) was added to viscous liquid acrylated oligomer and stirred thoroughly with a high speed rotating shaker and subsequently was subjected to solvent evaporation and degassing under reduced pressure. This is added into the Experimental Section. Round-shaped liquid films (ϕ = 10 mm) of comphorquinone-containing acrylated oligomers were irradiated with visible light. After immersion in dichloromethane to remove the soluble fraction, the insoluble polymer was dried and weighed. The photocuring yield was defined as the weight percentage of the insoluble part (W_g) against that of the initial prepolymer (W): $W_g/W \times 100$.

Water Contact Angle. The surface wettability of the photocured films was evaluated by measuring the static contact angles (advancing and receding) toward deionized water using the sessile drop method with a contact angle meter (CA-D, Kyowa Interface Co. Ltd., Tokyo, Japan) at 25 °C.

Hydrolytic Degradation. Photocured films (10 mm × 10 mm × 1 mm) were weighed (initial weight; W_O) and immersed in 0.01 M aqueous phosphate-buffered solution (PBS, pH 7.4) at 37 °C for up to 4 weeks under static conditions. After each 1-week period, the swollen weight (W_S) and dried weight (W_D) of the films were measured after wiping the surface with paper and after vacuum-drying, respectively. The weight loss (WL) and water adsorptivity (WA) upon hydrolysis on a weekly basis were evaluated as

$$\mathrm{WL}\,(\%) = 100([W_O - W_D]/W_O) \quad \text{and}$$

$$\mathrm{WA}\,(\%) = 100([W_S - W_D]/W_D)$$

Surface Topological Observation. The hydrolytic behavior of the photocured film surface was observed by scanning electron microscopy (SEM, JSM-840A, JEOL Ltd., Tokyo, Japan) after sputter-coating with gold and by atomic force microscopy (AFM, NBV100, Olympus Optical Co., Ltd., Tokyo, Japan; AFM controller & software, Nanoscope IIIa, Digital Instrument, NY). In AFM, the image was obtained by contact-mode scanning in PBS. A silicon−nitride soft cantilever with a spring constant of 0.027 N/m (Bio-lever, Olympus) was used to minimize the scanning-load-dependent geometric change, and the applied load was set to 0.8 nN.

Swelling Depth. Swelling depth was determined by a confocal laser scanning microscope (CLSM, Radiance 2000, Bio-Rad laboratories Inc., Hercules, CA). Each nonhydrolyzed and 4-week-hydrolyzed sample (5 mm × 5 mm × 1 mm) was immersed in aqueous rose bengal solution (10 mg/mL) for 2 days at 25 °C. The central part of the swollen specimen was sliced for visual observation of the cross section. The fluorescence intensity of the cross-sectional image was determined by NIH Image Software (version 1.58).

Microscopic Indentation Test. Two hundred microliters of prepolymer was coated on a glass dish (Iwaki Glass,

Scheme 1. Schematics of Preparation Routes of (Co)Oligomer and Acrylate-End-Capped Prepolymer and Photocuring.

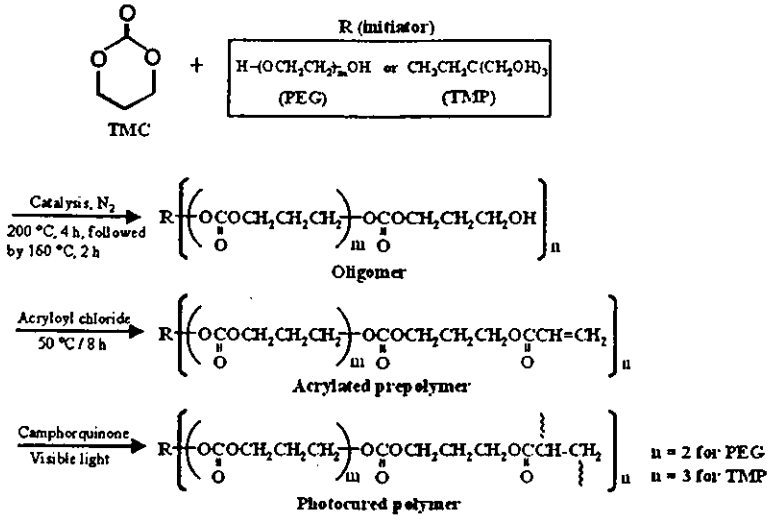

Japan; diameter of well = 15 cm, thickness of the well = ca. 1 mm), photocured, and then immersed in PBS. The AFM force−distance curves (f−d curves) of photocured samples were measured in the glass dish using a cantilever with a spring constant of 0.68 N/m at seven randomly chosen locations on each sample in PBS. The f−d curves were sequentially measured more than three times and typical curves were recorded by computer software after confirming the minimum fluctuations. The frequency of the tip approach/retract cycle was chosen to be 1.5 Hz to minimize the noise fluctuation in a single f−d curve. Raw f−d curves were converted to force-versus-indentation curves (F−δ curves).[20] Young's moduli of the surface of each sample were evaluated from the F−δ curves by fitting to a Hertz model.[20,21] Two kinds of model for fitting were employed, depending on the profile of the F−δ curve: a Hertz model for a conical tip (type A and B fittings) or for a flat-ended cylindrical tip (type C fitting) as described below (see Scheme 2).

Type A and B Fittings. For a conical tip with a semivertical angle α, the total force F as a function of the indentation δ is given as[20]

$$F_{\text{cone}}(\delta) = \frac{2\tan\alpha}{\pi}\frac{E}{1-\mu^2}\delta^2 \qquad (1)$$

where E is Young's modulus and μ is the Poisson ratio. The terms α and μ were 30° and 0.5, respectively.

Type C Fitting. A flat-ended cylindrical tip with radius R gives a linear F−δ relationship as[20]

$$F_{\text{cylinder}}(\delta) = 2RE\delta \qquad (2)$$

where R was 20 nm based on the radius of curvature of the tip (manufacturer's data).

Type A and B fitting analyses were performed on the F−δ^2 plot, while the type C fitting was used for the case in which the F−δ plot showed an almost linear profile. If the sample shows ideal homogeneous elasticity, the F−δ^2 plot would fit the linear profile in the case of a conical tip (type A fitting, see Scheme 2a). However, many samples typically exhibit nonlinear F−δ^2 plots with positive or negative curvatures. For the positive curvature, which is interpreted as the coupling of two lines with different slopes, the two-step fitting was adopted (type B fitting, see Scheme 2b). In the first step, a line fitting was applied to the initially indented region and the Young's modulus of the outermost surface region, E_1, was calculated from the slope. In the second step, a line fitting was performed for the fully indented region and Young's modulus of the subsurface, E_2, was calculated from the slope. The thickness of the highly swollen outermost surface (T) was evaluated from the intersection between the two-step fitting lines. On the other hand, for the negative curvature, linear fitting of an almost linear F−δ plot was adopted (type C fitting, see Scheme 2c). From the one-step fitting (type A and C fitting), Young's modulus (E) could be evaluated.

Statistical Analysis. All of the quantitative results were expressed as a mean ± SD. Statistical analysis was carried out using an ANOVA with a Scheffé test post hoc, $p < 0.05$. All statistical analyses were performed using Statview for Windows (SAS Institute, Inc., Copyright 1992−1998), version 5.0.

Results

Preparation of Liquid Acrylate-End-Capped TMC-Based Prepolymers. Scheme 1 illustrates the sequential reaction steps for preparation of a (co)oligomer, acrylation of (co)oligomer at both terminal ends, and photocuring. A series of TMC-based (co)oligomers was synthesized by ring-opening (co)polymerization in the presence of low molecular weight PEG (mol wt 200, 600, or 1000) or TMP as an initiator in the presence of stannic octanate as a catalyst. The PEG-initiated oligomer is linear, and the TMP-initiated oligomer has a three-armed branch. Table 1 summarizes the reaction conditions, monomer compositions, molecular weights, and the physical states of the (co)oligomers prepared. The compositions of (co)oligomers were determined by ^{1}H NMR spectroscopy (Figure 1a). The number-average molecular weights of the (co)oligomers, determined or estimated by GPC, ranged from approximately 650 to 3400. An increase in the ratio of monomer to initiator resulted in an increase in the number-average molecular weight of (co)oligomers,

Table 1. TMC-Based Biodegradable (Co)Oligomers[a]

monomer			monomer feed ratio		prepolymer composition[b]	molecular weight		physical state
M1	M2	initiator (I)	M1/M2/I	yield (%)	M1/M2/I	M_n	M_w/M_n	at 25 °C
TMC		PEG 1000	1:0:0.028	92.6	1:0:0.029	3380	2.01	viscous liquid
		PEG 1000	1:0:0.076	94.7	1:0:0.075	2240	1.84	liquid
		PEG 1000	1:0:0.100	94.5	1:0:0.107	1810	1.43	paste
		PEG 1000	1:0:0.250	92.5	1:0:0.268	1140	1.26	paste
		PEG 600	1:0:0.076	93.8	1:0:0.077	2180	1.59	liquid
		PEG 600	1:0:0.250	93.6	1:0:0.263	1040	1.48	liquid
		PEG 200	1:0:0.076	95.1	1:0:0.074	1630	1.52	viscous liquid
		PEG 200	1:0:0.250	93.4	1:0:0.247	650	1.36	liquid
		TMP	1:0:0.050	90.2	1:0:0.050	1690	1.68	viscous liquid
		TMP	1:0:0.167	94.4	1:0:0.168	920	1.42	liquid
TMC	L-lactide (LL)	PEG 1000	0.5:0.5:0.76	89.8	0.51:0.49:0.078	2410	1.27	liquid
		PEG 1000	0.5:0.5:0.250	84.4	0.63:0.37:0.313	1390	1.22	paste
		PEG 600	0.5:0.5:0.76	90.6	0.52:0.48:0.081	2370	1.49	viscous liquid
		PEG 200	0.5:0.5:0.76	88.7	0.52:0.48:0.086	2290	1.48	viscous liquid

[a] Reaction conditions were 200 °C for 4 h, followed by 160 °C for 2 h. [b] Determined by ^{1}H-NMR. [c] Determined by GPC in THF (PEG standard. M_n is number-average molecular weight; M_w is weight-average molecular weight; M_w/M_n is polydispersity. The molecular weight of the three-armed TMP-based oligomers estimated from the PEG standard, which is theoretically only applicable to linear polymers, may be overestimated because the hydrodynamic radius of a three-armed polymer is not the same as the linear polymer at the equivalent molecular weight basis.

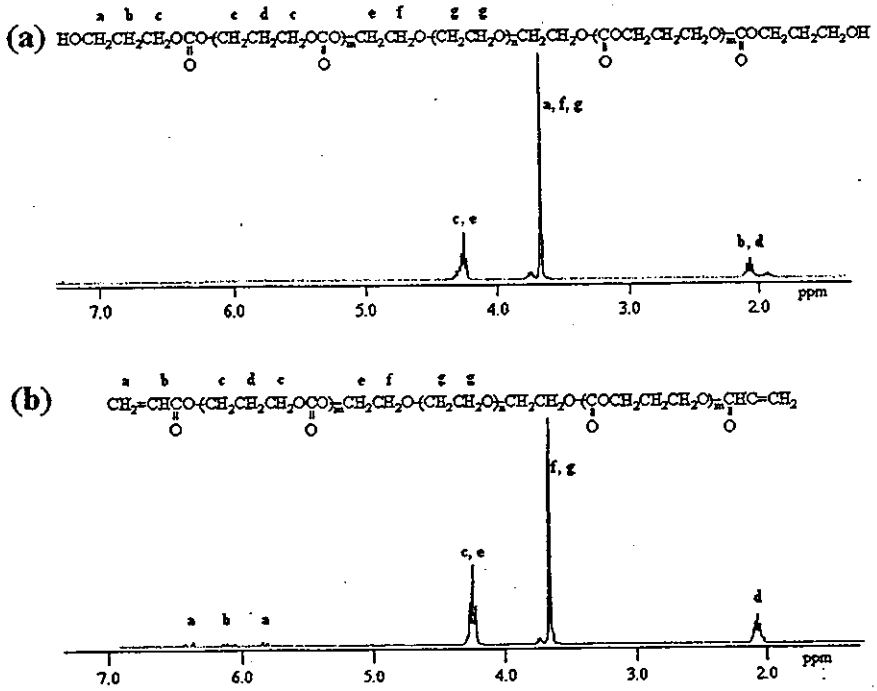

Figure 1. ^{1}H NMR spectrum and assignment of (a) (co)oligomer of PEG (molecular weight 1000) and TMC and (b) acrylate-end-capped prepolymer (**T/P1k**).

irrespective of the type of initiator. The yields of (co)-oligomers were approximately 85−95 wt %. The (co)-oligomer compositions were almost identical to those of the initial feeds. The resultant (co)oligomers were pastes, viscous liquids, or liquids at room temperature, depending on the monomer composition and the molar ratio of monomer to initiator. Among these (co)oligomers, several liquid (co)-oligomers were subjected to further acrylate end-capping by esterification using excess acryloyl chloride against the hydroxyl groups of the terminal ends of (co)oligomers. As shown in Table 2, 90−98% esterification was achieved, which was determined by ^{1}H NMR spectroscopy (Figure 1b). All of the acrylate-end-capped prepolymers thus prepared were liquid [the code names of photocurable prepolymers such as **T/P1k**, **T/P200**, **T/TMP**, and **T/L/P1k** are in Table 2. T and L denote TMC and LL, respectively. P1k and P200 denote PEG with mol wt of 1000 and 200, respectively].

Photocuring Characteristics. Photopolymerization was carried out by visible light (xenon lamp with UV and IR cutoff filters) as a light source in the presence of camphorquinone as an initiator. The photocured polymers, which were not soluble in any organic solvent, were obtained, irrespective of the type of prepolymers. The dependence of photocuring characteristics on light intensity, camphorquinone concentration, liquid film thickness, and composition of prepolymer was systematically determined (Figure 2).

The effect of visible-light intensity on the irradiation time-dependent photocuring yield of **T/P1k** (Table 2) at a fixed

Table 2. Acrylate-End-Capped Liquid Biodegradable Prepolymers and the Surface Wettabilities of Photocured Films

		acrylate-end-capped prepolymer[a]		photocured films[b]		
prepolymer code	initiator	TMC/lactide/intiator	degree of acrylation (%)	gel yield (%)	advancing contact angle[c] nonhydrolyzed/ 4 weeks hydrolyzed	receding contact angle[c] nonhydrolyzed/ 4 weeks hydrolyzed
T/P1k	PEG 1000	1:0:0.076	97	92.7	23.8 ± 1.62/24.1 ± 1.88	<5.0/<5.0
T/P200	PEG 200	1:0:0.250	90	97.9	41.5 ± 2.55/42.2 ± 0.94	27.0 ± 3.56/13.0 ± 1.69
T/TMP	TMP	1:0:0.167	92	97.8	59.2 ± 1.50/61.6 ± 1.25	47.4 ± 5.33/28.5 ± 1.90
T/L/P1k	PEG 1000	0.5:0.5:0.076	94	90.4	32.3 ± 4.47/74.4 ± 1.85	9.7 ± 1.74/11.7 ± 1.16

[a] Determined by ^{1}H-NMR. [b] Photocuring conditions were liquid film of acrylate-end-capped prepolymers of thickness 1 mm under photoirradiation at the intensity of 100 mW/cm^2 for 1 min at room temperature with a camphorquinone concentration of 0.5 wt % of prepolymer. [c] Advancing and receding water contact angle measured using deionized water by the sessile drop method.

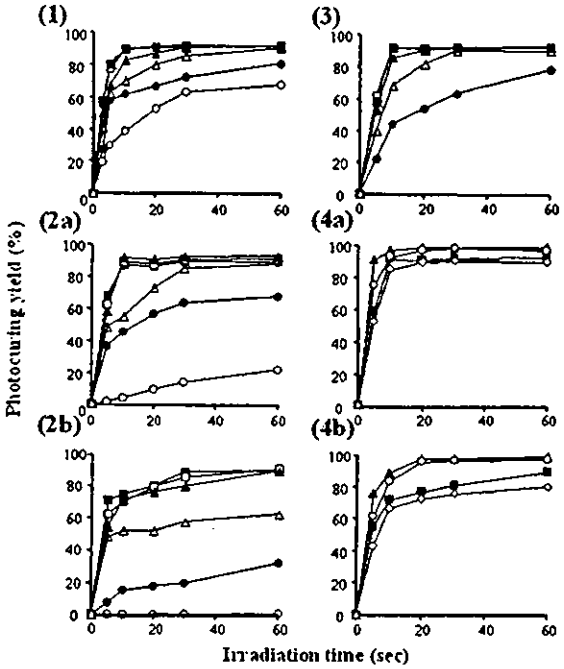

Figure 2. Dependence of photocuring yield of liquid acrylate-end-capped prepolymer films on photopolymerization conditions as a function of photoirradiation time: (1) effect of visible-light intensity on photocuring of **T/P1k** film (1 (○), 5 (●), 20 (△), 50 (▲), 100 (□), and 200 (■) mW/cm^2; camphorquinone concentration = 0.5 wt %; liquid film thickness = 1 mm); (2) effect of camphorquinone concentration on photocuring of **T/P1k** film (0 (○), 0.05 (●), 0.1 (△), 0.3 (▲), 0.5 (□), and 1 (■) wt %; light intensity = 100 mW/cm^2 (a) or 20 mW/cm^2 (b); liquid film thickness = 1 mm; (3) effect of liquid film thickness on photocuring of **T/P1k** film (1 (■), 3 (□), 5 (▲), 10 (△), and 20 (●) mm; light intensity = 100 mW/cm^2; camphorquinone concentration = 0.3 wt %); (4) effect of types of prepolymers on photocuring (**T/P1k** (■), **T/P200** (○), **T/TMP** (▲), and **T/L/P1k** (◇); light intensity = 100 mW/cm^2 (a) or 20 mW/cm^2 (b); camphorquinone concentration = 0.3 wt %; liquid film thickness = 1 mm.

concentration of camphorquinone (0.5 wt %) is shown in Figure 2-1. The yield increased with both irradiation time and light intensity. At higher light intensity (100 and 200 mW/cm^2), there was little difference in the photocuring kinetic characteristics, reaching a photocuring yield of approximately 90% within 10 s. The effect of camphorquinone concentration on the irradiation-time-dependent photocuring yield of **T/P1k** at the light intensities of 100 and 20 mW/cm^2 is shown in Figure 2-2a,2b, respectively. When camphorquinone concentration was increased, the yield increased with irradiation time. This tendency was more profound for high light intensity than low light intensity. For example, even in the absence of camphorquinone, photocuring yield increased with irradiation time at 100 mW/cm^2, whereas little photocured gel was produced at 20 mW/cm^2. At higher concentrations of camphorquinone, above 0.3 wt %, irrespective of light intensity, almost the same irradiation time dependence of photocuring yield was obtained. The effect of the liquid film thickness of the prepolymer **T/P1k** on irradiation-time dependence of photocuring yield was examined at liquid film thicknesses ranging from 1 to 20 mm. Below 10 mm thickness, over 90% of photocuring occurred within 30 s of photoirradiation as shown in Figure 2-3. The dependence of photocuring yield on irradiation time for different acrylate-end-capped prepolymers at high (100 mW/cm^2) and low (20 mW/cm^2) intensities is shown in Figure 2-4a,4b, respectively. The higher molecular weight prepolymers showed slightly lower photocuring characteristics, as shown in Figure 2-4a: yield of all of the prepolymers was above 90 wt % within 10 or 20 s at high-intensity irradiation (100 mW/cm^2).

Surface Wettability. The water contact angles (advancing and receding) of photocured polymer films before and after 4-week immersion in PBS are shown in Table 2. Before immersion into PBS, photocured polymers, P(**T/P1k**) and P(**T/L/P1k**), both of which were obtained using PEG1000 as an initiator, exhibited quite low advancing and receding angles, indicating that these photocured films were highly wettable. On the other hand, P(**T/P200**) film, obtained using PEG200, exhibited moderately low contact angles, whereas P(**T/TMP**) exhibited relatively high contact angles. Upon 4-week immersion in PBS, there were little differences in the advancing angles of photocured polymers except for P(**T/L/P1k**), which exhibited elevated advancing angles. Irrespective of type of photocured copolymers, quite low receding contact angles were noted.

Hydrolysis Characteristics. The hydrolytic characteristics of the photocured polymer films immersed in 0.01 M PBS at 37 °C were determined by several techniques: (I) weight loss and water uptake, (II) surface topological observations, (III) swelling depth, and (IV) changes of surface elastic properties.

Characterization of Hydrolytic Behavior (I): Weight Loss and Water Uptake. Figure 3 shows the dependence of weight loss (a) and water uptake (b) on time for films of four photocured polymers [P(**T/P1k**), P(**T/P200**), P(**T/TMP**), and P(**T/L/P1k**)]. Irrespective of the type of photocured polymer, the weight loss of the films gradually increased with immersion time. At 4 weeks of immersion, the films of P(**T/P200**) and P(**T/TMP**) showed weight losses of 4.3%

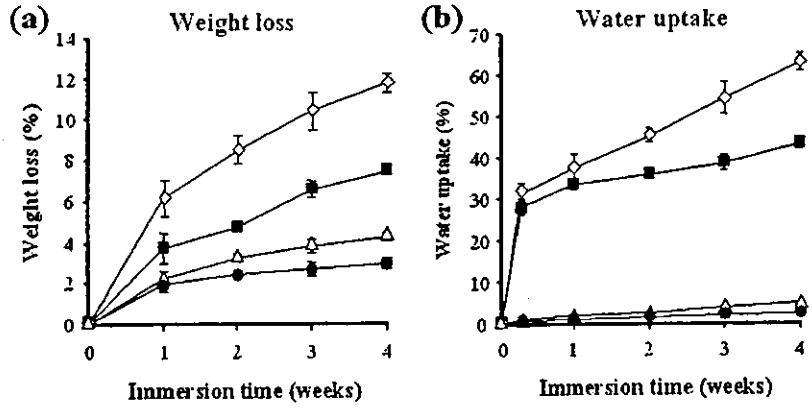

Figure 3. Weight loss (a) and water uptake (b) of photocured polymer films P(T/P1k (■), P(T/P200) (△), P(T/TMP) (●), and P(T/L/P1k) (◇) during degradation (n = 3).

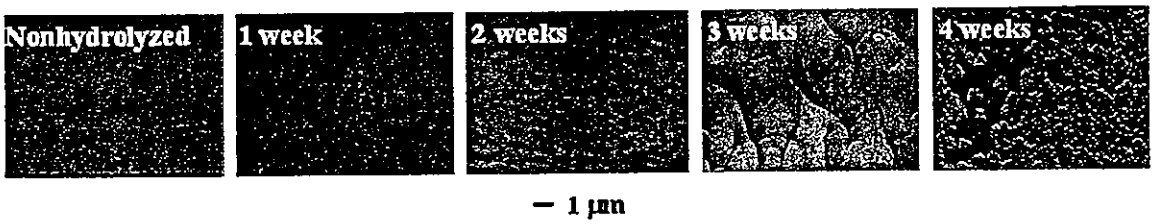

Figure 4. SEM images of photocured polymer, P(T/P1k), films for up to 4 weeks of immersion in PBS at 37 °C.

and 2.9%, respectively. PEG1000-based polymers, P(T/P1k)- and P(T/L/P1k), exhibited higher degradation rates than the former two photocured polymers: for example, weight loss after 4-week immersion of P(T/L/P1k) film was approximately 12%, which is almost four times larger than that of P(T/TMP). Initial two-day water uptakes of these PEG1000-based polymer films were about 30% and gradually increased with immersion time, while those of P(T/P200) and P(T/TMP) films were less than 5% even at 4 weeks of immersion.

Characterization of Hydrolytic Behavior (II): Surface Topological Observation. To characterize the topographical surface changes of the photocured polymer films subjected to hydrolysis, microscopic observations with SEM and AFM were performed. SEM images of P(T/P1k) films subjected to hydrolysis P(T/P200) for up to 4 weeks are shown in Figure 4. After being dried under vacuum for SEM observation, the films exhibited significant cracks on their surfaces after 3- and 4-week immersions, whereas much less hydrolyzable P(T/P200) film showed very smooth surfaces during the entire observation period (data are not shown), indicating that the dried P(T/P1k) film surface became roughened with immersion time. The AFM observation in PBS clearly showed the microtopological changes of the swollen surface of P(T/P1k) film during 6 weeks of hydrolysis as follows. Figure 5a,b shows height images of the film at different immersion periods and its cross-sectional analysis, respectively. At 5 h and 1 week of immersion, the film showed a slightly rough surface (roughness around 10 nm in height) probably due to irregular swelling of the surface with inhomogeneous morphological state. At 2 weeks of immersion, the surfaces became relatively smooth, suggesting that the swollen layer was flattened during this period. After 4 weeks of immersion, small indents or pits on the film surface probably caused by local erosion were observed, which were enlarged after further immersion (6 weeks). The depth of pits reached approximately 20 nm.

Characterization of Hydrolytic Behavior (III): Swelling Depth. The swelling depth profile of the photocured polymer films was determined by CLSM upon staining with aqueous rose bengal solution. For the photocured PEG1000-based polymers [P(T/P1k) and P(T/L/P1k)], the slices of films were uniformly and completely stained with the dye even before being subjected to hydrolysis, indicating that these films were already highly swollen prior to hydrolysis (Figure 6a). On the other hand, P(T/P200) and P(T/TMP) films exhibited a slight staining only on their outermost surface regions, both before and after hydrolysis. Figure 6b shows the depth profile of fluorescence intensity in the cross section of the films of P(T/P200) and P(T/TMP) before hydrolysis and after 4-week hydrolysis. In the nonhydrolyzed P(T/P200), although the fluorescence intensity and depth distribution, which reflect the degree of swelling, increased after 4 weeks of hydrolysis, swelling was limited to the outermost surface region but proceeded to deeper regions with immersion time. The least swellable photocured polymer, P(T/TMP), exhibited much less dye uptake and smaller depth of dye-stained section than those of P(T/P200). There was little difference in maximal fluorescent intensity and width between nonhydrolyzed and 4-week hydrolyzed P(T/TMP).

Characterization of Hydrolytic Behavior (IV): Surface Elastic Property. Micromechanical properties of the swollen surface region were determined using the microscopic indentation test by AFM in PBS. Figure 7 shows force–indentation curves ($F-\delta$ plots) of photocured polymers [P(T/P1k), P(T/P200), and P(T/TMP)], which were subjected to hydrolysis for up to 6 weeks in PBS. For the whole-body-swellable polymer, P(T/P1k), a marked time-dependent change in the $F-\delta$ curve was noticed. The indentation depth gradually increased with immersion time. Such a trend with

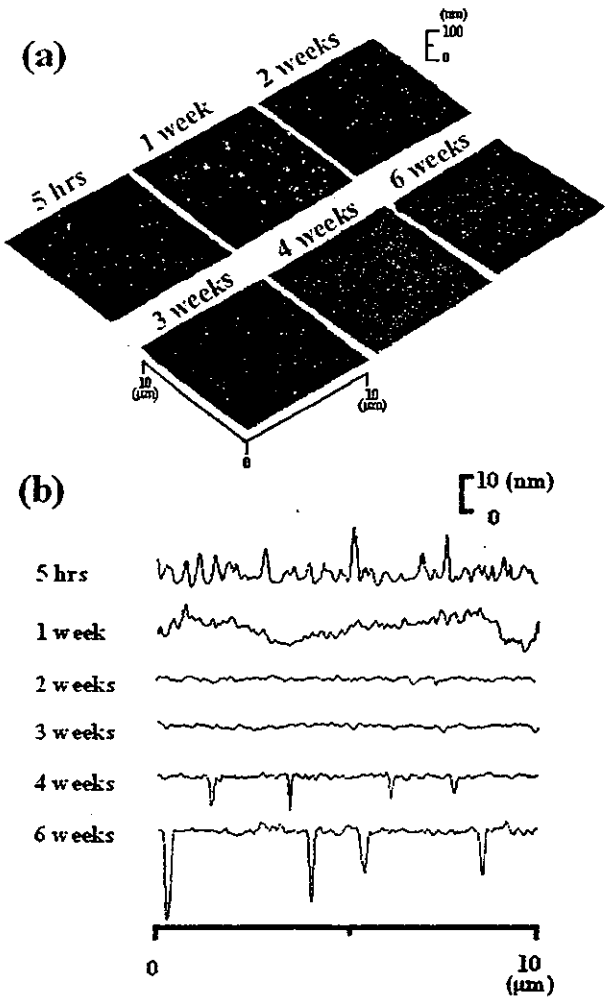

Figure 5. AFM (a) height images of photocured polymer (P(T/P1k)) films for up to 6 weeks of immersion in PBS at 37 °C and (b) section analysis of hydrolyzed polymer films.

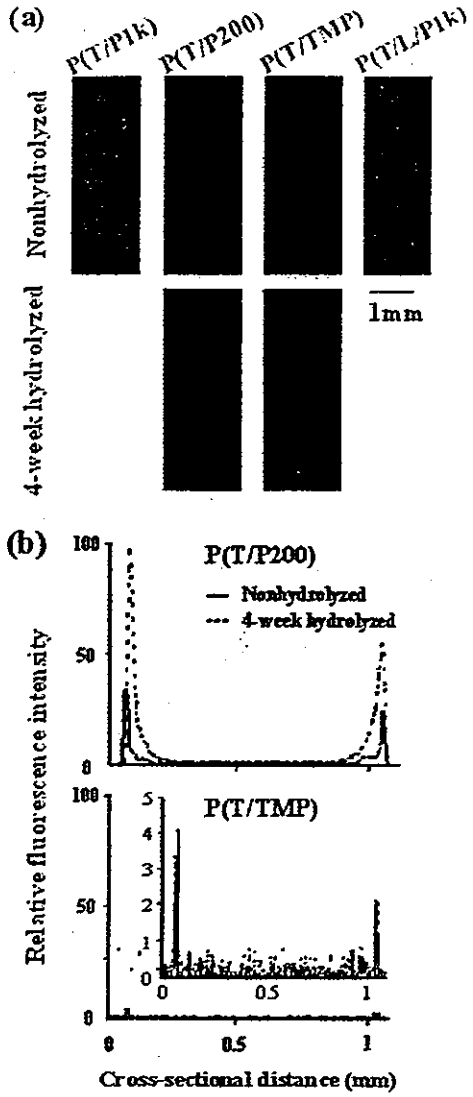

Figure 6. Distribution of fluorescence (a) at cross sections of nonhydrolyzed and 4-week hydrolyzed photocured polymer films stained with aqueous rose bengal solution and (b) fluorescence intensity distribution in cross sections of stained P(T/P200) and P(T/TMP)) films before (line) and after (dashed line) hydrolysis (n = 5).

less change was also observed for P(**T/P200**) the swelling of which was limited only to the surface region (Figure 6). In the case of the least swellable polymer, P(**T/TMP**), a minimal increase in indentation depth was observed during 6 weeks of immersion.

To quantify the elastic properties of the photocured polymers, fitting analyses employing Hertz models were performed according to the methods shown in Scheme 2. If the elastic property of the polymer obeys an "ideal" Hertz model for a conical tip, $F-\delta^2$ plots should have a linear profile (type A fitting in Figure 8b). However, many real $F-\delta^2$ plots exhibited significant curvatures: positive or negative except for those listed below, 4- and 6-week-immersed P(**T/P1k**) and 5-h- and 1-week-immersed P(**T/P200**) (Figure 8a). Positive curvature suggests that a higher index of δ is required to fit the original $F-\delta$ plot appropriately. However, index "2" for a conical-shaped tip is theoretically the highest one in the Hertz model. We interpreted such nonideal behavior of the $F-\delta^2$ plot as the coupling of the two linear parts, that is, two-step fitting (type B fitting in Figure 8b), which is caused by two heterogeneous layers at the surface region. On the other hand, the slightly negative curvature of the $F-\delta^2$ plot (plots of P(**T/P1k**) film after 5-h, 1-week, and 2-week hydrolyses, in which the slope of the initially indented region is steeper than that of the fully indented region) means that the original $F-\delta$ plot is more similar to a linear profile than to a quadratic profile. In this case, index "1" for the cylindrical tip Hertz model should be applied for fitting (type C fitting in Figure 8b).[20,21]

From the two-step fitting analysis for the $F-\delta^2$ plot with positive curvature (type B fitting), the slopes of the fitted lines for the initially indented region and for the fully indented region can be determined to give Young's moduli of the outermost surface region (E_1) and subsurface (E_2), respectively. In addition, from the intersection point between these two fitted lines, we deduced the characteristic thickness of the highly swollen outermost surface (T) taking into account that the significant change in elastic property was observed around the intersection point. Young's modulus (E) can only be evaluated for the surface of relatively thick mechanically uniform films from the fitting analysis of the $F-\delta^2$ plot with a linear equation (type A fitting) and the $F-\delta$ plot with a linear equation for the cylindrical tip (type C fitting).

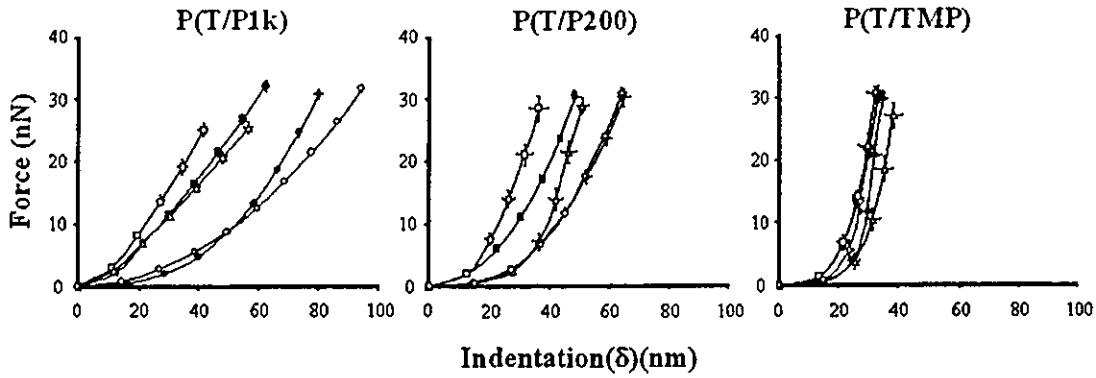

Figure 7. Force–indentation curves (F–δ curves) of photocured polymer (P(**T**/P1k), P(**T**/P200), and P(**T**/TMP)) films: 5 h (■), 1 week (□), 2 weeks (△), 4 weeks (●), and 6 weeks (○) of immersion in PBS ($n = 7$).

Scheme 2. Methods of Fitting Analyses of Nanoscopic Force–Indentation Curves by Hertz Models (1) for a Conical Tip with (a) Linear Fitting for F–δ^2 Plot (Type A Fitting) or (b) Two-Step Fitting for Biphasic F–δ^2 Plot (Type B Fitting) and (2) for a Flat-Ended Cylindrical Tip with (c) Linear Fitting for F–δ Plot (Type C Fitting)[a]

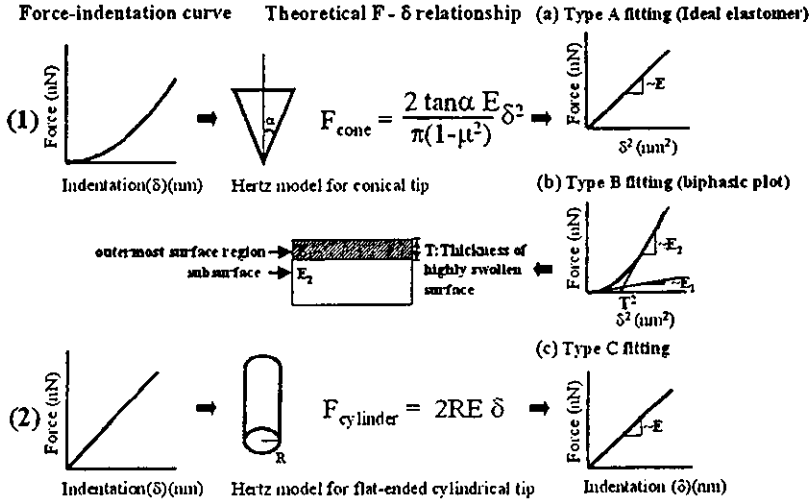

[a] The symbols are described in the Experimental Section.

Figure 9 shows hydrolysis time-dependent averaged E (calculated by the method described above) for the uniform surfaces and E_1 and E_2 for the mechanically biphasic-layered surfaces ($n = 7$). The most water-swellable polymer, P(**T**/**P1k**), exhibited a very low E ($E_1 = E_2$) of approximately 10 MPa, which tended to decrease with time (calculated using type C fitting for the early period and type A fitting for the later period). The less water-swellable polymer, P(**T**/**P200**), exhibited a linear F–δ^2 plot (type A fitting) at the very early stage of immersion but a biphasic plot (type B fitting) in the later period. A relatively large E was observed for an early period of hydrolysis; however, quite low E_1 (around 10 MPa, irrespective of immersion time) and reduced E_2 (around 40 MPa at 2 weeks and around 20 MPa at 4 and 6 weeks) were observed for a later period. Young's modulus tended to decrease with hydrolysis time. The least swellable polymer, P(**T**/**TMP**), exhibited a biphasic F–δ^2 plot: fairly large E_1 and large E_2. E_1 tended to decrease with time, whereas E_2 increased particularly at the later period of hydrolysis. Generally, E_2 was larger than E_1 for both P(**T**/**P200**) and P(**T**/**TMP**), indicating that the outermost surface region became softer than the bulk phase upon hydrolysis. As for the comparison of elasticities of different photocured polymer films at the surface region, Young's modulus increased in the following order: P(**T**/**P1k**) < P(**T**/**P200**) ≪ P(**T**/**TMP**) for any duration of hydrolysis.

Figure 10 shows the thickness (T) of the highly swollen outermost surface region for both P(**T**/**P200**) and P(**T**/**TMP**), which were determined from the intersection point in the type B fitting. The calculated thickness of P(**T**/**P200**) was approximately 40 nm at 2–6 weeks of immersion, while P(**T**/**TMP**) had a thickness of almost 25–28 nm during the entire course of hydrolysis up to 6 weeks.

Discussion

Liquid acrylated oligo(ester)- or oligo(carbonate)-based prepolymers with the ability to rapidly transform into a solid upon visible-light photoirradiation may find various medical applications such as drug delivery matrixes, photoconstructs of microarchitectural surfaces, micro- and macroshaped devices for implants and engineered tissues, and in situ formable molds. In our previous studies, liquid acrylated prepolymers composed of TMC and CL were prepared. The polymer composition, type of alcohol used as an initiator, its functionality-differentiated surface erosion rate, and the concomitant biodegradability of the photocured implants were reported.[9,19]

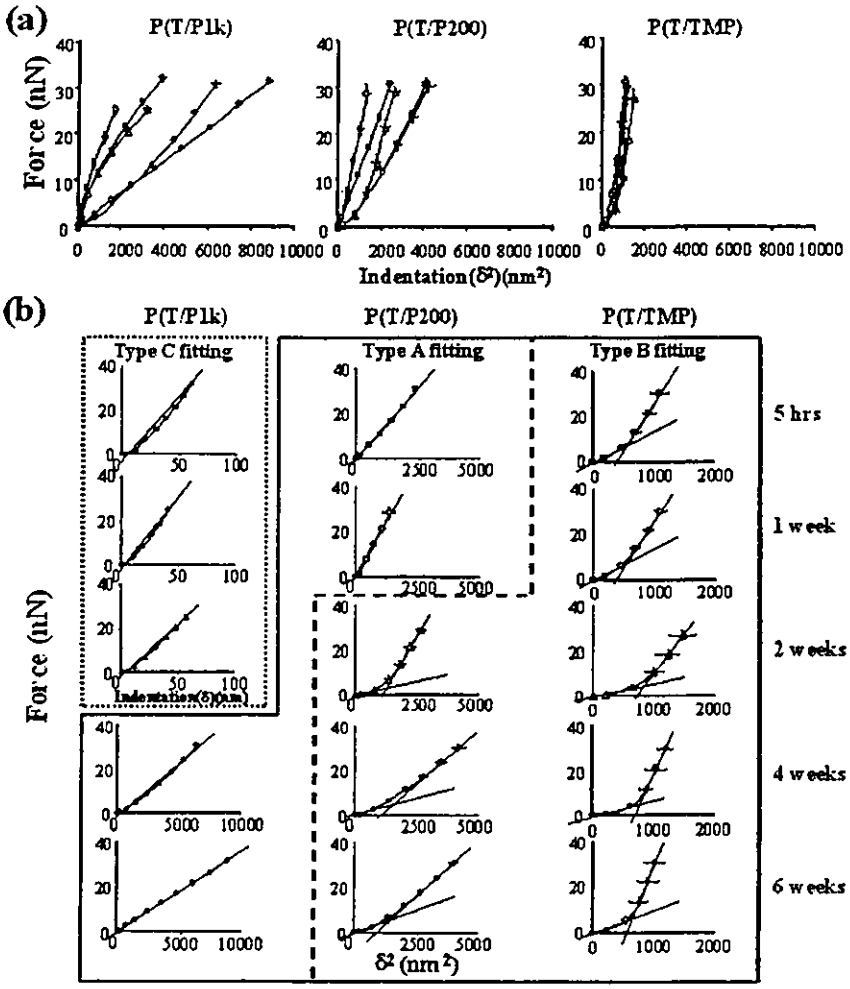

Figure 8. $F-\delta^2$ plots (a) for the analysis with Hertz model for 5 h (■), 1 week (□), 2 weeks (△), 4 weeks (●), and 6 weeks (○) of immersion in PBS and (b) three types of fitting analyses with Hertz model: linear fitting for linear $F-\delta^2$ plots using conical tip assumption (type A fitting), a biphasic fitting for biphasic $F-\delta^2$ plots using conical tip assumption (type B fitting), and linear fitting for $F-\delta$ plots using the model of a flat-ended cylindrical tip (type C fitting) ($n = 7$).

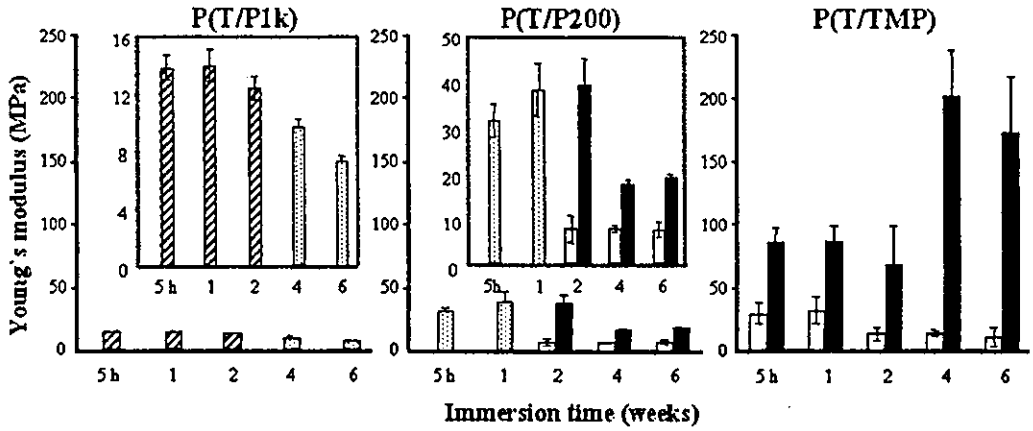

Figure 9. Young's moduli of P(T/P1k), P(T/P200), and P(T/TMP) films upon hydrolysis ($n = 7$).

In this study, we focused on the preparation of various types of liquid acrylated TMC-based prepolymers using triol (TMP) and linear PEGs with molecular weights of 200, 600, or 1000. The former prepolymer is trifunctional acrylated prepolymer, whereas the latter prepolymers are bifunctional acrylated prepolymers. The resultant acrylated prepolymers have molecular weights of between 800 and 2600. In the case of trifunctional prepolymer, T/TMP, the molecular weight, as obtained from standard GPC calibrated with well-defined linear PEGs, could be lower than its true molecular weight because the hydrodynamic volume of a branched molecule is smaller than that of a linear one.[22] Depending on the type of initiator and its molecular weight, comonomer, and polymer composition, the physical state of the (co)-oligomers was liquid, viscous liquid, or paste (Table 1). Upon acrylation at terminal ends of liquid (co)oligomers, acrylated

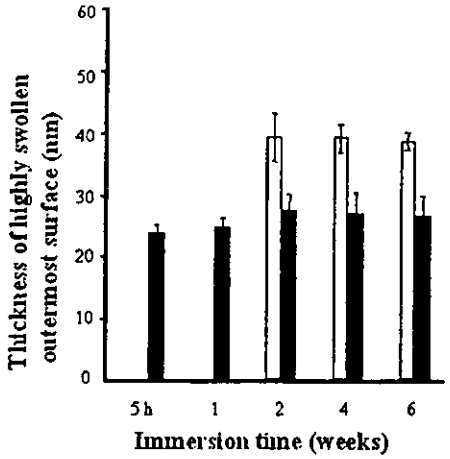

Figure 10. Thickness of the highly swollen outermost surface (T) calculated at the intersection of two-step fitting lines of the biphasic $F-\delta^2$ plot ($n = 7$).

prepolymers exhibited a rapid liquid-to-solid transformation induced by visible-light irradiation, irrespective of the type of prepolymers studied here. All of the acrylated prepolymers photocured within 10−20 s of photoirradiation at the photointensity (100 mW/cm^2) used (Figure 2). The photocuring yield increased with increasing irradiation time, photointensity (Figure 2-1), and camphorquinone concentration (Figure 2-2) but tended to decrease with increasing liquid film thickness (Figure 2-3) and molecular weight of prepolymer (Figure 2-4). These photocuring characteristics were similar to those of polymers composed of TMC and CL, which were reported in our previous paper.[19]

The wettability and time-dependent characteristics of water uptake and weight loss during hydrolysis depended on the type of photocured polymer (Figure 3). As expected, the higher degrees of water uptake and weight loss were found for P(**T/L/P1k**), followed by P(**T/P1k**), compared with P(**T/P200**) and P(**T/TMP**), indicating that the hydrophilic component as an initiator, PEG1000, and faster degradable polyester, PLL, than polycarbonate are responsible for this behavior. The PEG200-based polymer, P(**T/P200**), exhibited moderate degrees of this behavior. The lowest degrees of this behavior were observed for TMP-based P(**T/TMP**), which lacks a hydrophilic component in the molecule and heavier cross-linking density due to trifunctional prepolymer compared with bifunctional PEG-based prepolymers (Figure 3). Topological SEM and AFM images of hydrolyzed surfaces of photocured films and swelling depth profiles of cross-sectional views of rose bengal-stained samples by CLSM clearly differentiated the hydrolytic degradation behavior of these photocured polymers. The results are summarized as follows. (1) For P(**T/P1k**), a highly swollen rough layer was formed at an early period of immersion in water, but it became smoother upon further immersion. However, at a prolonged period, pits were created, probably due to the inhomogeneous surface composition (Figure 5). (2) The swelling and subsequent hydrolysis occurred only at the surface region of the photocured polymers P(**T/P200**) and P(**T/TMP**), whereas P(**T/P1k**) exhibited complete swelling of the sample (Figure 6).

It is of great interest to determine how micromechanical properties of surface regions of photocured polymers are changed upon hydrolysis and their dependences on the type of photocured polymers. The force−indentation curves determined by nanoindentation using AFM differentiated the nature of water-swellable surface regions and concomitantly the microelastic modulus of the surface regions. Qualitatively, there were marked differences between the hydrolysis-time-dependent force−indentation curves of hydrolyzed samples (Figure 7). Regardless of the hydrolysis time, indentation was enhanced in the order P(**T/P1k**) > P(**T/P200**) ≫ P(**T/TMP**). P(**T/P1k**) became significantly softer with a hydrolysis time increase. This tendency was also observed for both P(**T/P200**) and P(**T/TMP**). However, the tendency was reduced in the order P(**T/P1k**) > P(**T/P200**) ≫ P(**T/TMP**).

For quantitative discussion, the Hertz model was employed to determine the microelastic modulus. The linear $F-\delta^2$ relation, from which Young's modulus is determined, was obtained when a cone-type tip was used for measurement (type A fitting in Scheme 2). This was observed for P(**T/P200**) during the early period of hydrolysis. However, a concave $F-\delta^2$ relation was observed during the later period of hydrolysis. This strongly implies that surface regions are inhomogeneous in the vertical direction of surface (depth). The concave curve is divided approximately into two linear fittings. This means that a two-layer surface model (Figure 8b) approximately fits the $F-\delta^2$ curves. This allows the differentiation of the microelastic modulus of surface regions. Young's moduli at the outermost surface regions were much smaller than those at deeper regions. The approximate thickness of the highly swollen layer, which was calculated from the intersection points of two linear lines, was estimated to be approximately 40 nm, which did not change over an observation period for up to 6 weeks. This also occurred in P(**T/TMP**), which swelled only at the outermost surface region: the thickness of the surface region with low elastic modulus was estimated to be 25−30 nm, which did not change considerably even with longer term hydrolysis (Figure 10). Taken together, these factors indicate that, for both P(**T/TMP**) and P(**T/P200**), degradation proceeds via a surface erosion. The increased E_2 (Young's modulus of the deeper or less swellable layer) of P(**T/TMP**) observed at after a longer period of hydrolysis, as shown in Figure 9, may be due to the effect of oxygen during photopolymerization. Oxygen, diffused into the surface regions, retards or inhibits radical polymerization, resulting in a lower cross-linking density at the outer surface region than at the deeper surface region or in the bulk phase. On the other hand, as for P(**T/P1k**), type C fitting was employed for an early period of hydrolysis, whereas type A fitting was for a later period. At this moment, we do not have any reasonable interpretation for a type C fitting (that is a linear $F-\delta$ relation) during an early period despite use of a cone-type tip in the AFM measurement. (Note that theoretically the type C fitting is observed using the flat-ended cylindrical-type AFM tip.) Regardless of the type of curve fitting, Young's moduli tended to decrease as the hydrolysis period lengthened. The estimated Young's moduli were as follows: for the highly swellable surface of P(**T/P1k**), E ($E_1 = E_2$) was almost 10 MPa; for the less swellable surface of P(**T/P200**), E_1 was approximately 10 MPa and E_2 ranged from 40 MPa (initial

period) to 20 MPa (later period); for the least swellable P(T/TMP), E_1 was 35 MPa (initial) to 15 MPa (later), and E_2 was approximately 100 MPa (initial) to 200 MPa (later).

The combination of a biodegradable liquid prepolymer with a photocured polymer having a wide scope of hydrolytic characteristics including surface erosion or whole-body degradation may provide a unique opportunity for the design of a drug-controlled-release matrix, in situ formable scaffold, and the fabrication of precision surface architectures or microdevices using a stereolithographic technique. These will be reported soon.

Acknowledgment. This study was financially supported in part by a Grant-Aid for Scientific Research (Grants A2-12358017 and B2-12470277) from the Ministry of Education, Culture. Sports, Science, and Technology of Japan.

References and Notes

(1) Vert, M. *Angew Makromol. Chem.* **1989**, *166*, 155.
(2) Langer, R.; Vacanti, J. P. *Science* **1993**, *260*, 920.
(3) Okada, H.; Yamamoto, M.; Heya, T.; Inoue, Y.; Kamei, S.; Ogawa, Y.; Toguchi, H. *J. Controlled Release* **1994**, *28*, 121.
(4) Piskin, E. *J. Biomater. Sci. Polym. Ed.* **1994**, *6*, 775.
(5) Chiellini, E.; Solaro R. *Macromol. Symp.* **1995**, *98*, 803.
(6) Mooney, D. J.; Mazzoni, C. L.; Breuer, C.; McNamara, K.; Hern, D.; Vacanti, J. P.; Langer, R. *Biomaterials* **1996**, *17*, 115.
(7) Hubbell, J. A. *Solid State Mater. Sci.* **1998**, *3*, 246.
(8) Hubbell, J. A. U.S. Patent 6,306, 922, October, 2001.
(9) Mizutani, M.; Matsuda, T. *J. Biomed. Mater. Res.* **2002**, *62*, 395.
(10) Cooke, M. N.; Fisher, J. P.; Dean, D.; Rimnac, C.; Mikos, A. G. *J. Biomed. Mater. Res., Part B: Appl. Biomater.* **2002**, *64B*, 65.
(11) Zhu, K. J.; Hendren, R. W.; Jensen, K.; Pitt, C. G. *Macromolecules* **1991**, *24*, 1736.
(12) Albertsson, A.-C.; Sjöling, M. *J. Polym. Sci., Pure Appl. Chem.* **1992**, *A29*, 43.
(13) Albertsson, A.-C.; Eklund, M. J. *Appl. Polym. Sci.* **1995**, 57, 1, 87.
(14) Matsuda, T.; Mizutani, M. *Macromolecules* **2000**, *33*, 791.
(15) Matsuda, T.; Mizutani, M.; Arnold, S. C. *Macromolecules* **2000**, *33*, 795.
(16) Mizutani, M.; Matsuda, T. *Biomacromolecules* **2002**, *3*, 249.
(17) Matsuda, T.; Mizutani, M. *J. Biomed. Mater. Res.* **2002**, *61*, 53.
(18) Matsuda, T.; Mizutani, M.; Arnold, S. C. *Biomacromolecules* **2002**, *3*, 668.
(19) Matsuda, T.; Mizutani, M. *J. Biomed. Mater. Res.* **2002**, *62*, 387.
(20) Weisenhorn, A. L.; Khorsandi, M.; Kasas, S.; Gotzos, V.; Butt, H.-J. *Nanotechnology* **1993**, *4*, 106.
(21) Sneddon, I. N. *Int. J. Eng. Sci.* **1965**, *3*, 47.
(22) Benoît, H.; Grubisic, Z.; Rempp, P.; Decker, D.; Zilliox, J. G. *J. Chim. Phys.* **1966**, *63*, 1507.

BM034231K

TISSUE ENGINEERING
Volume 10, Number 3/4, 2004

Photocured, Styrenated Gelatin-Based Microspheres for *de Novo* Adipogenesis through Corelease of Basic Fibroblast Growth Factor, Insulin, and Insulin-Like Growth Factor I

TEIICHI MASUDA, M.D.,[1,2] MASUTAKA FURUE, M.D., Ph.D.,[2] and TAKEHISA MATSUDA, Ph.D.[1]

ABSTRACT

***De novo* adipose tissue formation appears to proceed via two different biological events: neovascularization and spontaneous accumulation of preadipocytes and subsequent differentiation to mature adipocytes. In this article, we perform accelerated *de novo* adipose tissue engineering using photocured, styrenated, gelatin-based microspheres (SGMs) with different drug release rates of immobilized angiogenic and adipogenic factors. The concept of this system is to induce neovascularization and migration of endogenous preadipocytes by the rapid delivery of the angiogenic factor basic fibroblast growth factor (bFGF), followed by the proliferation and differentiation of preadipocytes into adipocytes by the prolonged delivery of the adipogenic factors, insulin and insulin-like growth factor I (IGF-I). Bioactive substance-immobilized SGMs with different drug release rates were prepared with different gelatin concentrations. An *in vitro* study showed the prolonged release of an immobilized model protein and the dependence of drug release rate on gelatin concentration. After the subcutaneous injections of SGMs immobilized with these bioactive substances in different combinations, the formation of masses or clusters of adipocytes was observed in rats. Triglyceride content in the injection site for the group that received bFGF-, insulin-, and IGF-I-immobilized SGMs was significantly higher than that for the group that received insulin- and IGF-I-immobilized SGMs 4 weeks after the injection of microspheres. These results suggest that the system developed here is effective for the *de novo* formation of adipose tissue as it enables the induction of the two-step biological reaction by single injection.**

INTRODUCTION

SOFT TISSUE AUGMENTATION is still an ongoing challenge in the field of plastic and reconstructive surgery. The use of adipose tissue equivalents is required for the treatment of soft tissue defects such as congenital malformations (e.g., hemifacial microsomia and Poland's syndrome) and posttraumatic or postoperative wounds. The available clinical approaches to overcoming these issues include local–regional or free microvascular flaps, dermal fat graft, collagen injection, the use of synthetic materials, and autologous fat transplantation. Each of these methods, however, is associated with certain drawbacks such as operative risk to some degree, donor site morbidity, resorption of implanted grafts, and foreign body reaction to the implanted synthetic materials.[1–4]

The tissue-engineering approach to forming adipose

[1]Department of Biomedical Engineering, Graduate School of Medicine, Kyushu University, Fukuoka, Japan.
[2]Department of Dermatology, Graduate School of Medicine, Kyushu University, Fukuoka, Japan.

tissue can be realized via two methods: one method is to transplant preadipocytes with or without a scaffold into the site in which soft tissue repair is required, followed by the spontaneous differentiation of preadipocytes or adipocyte progenitor cells to mature adipocytes,[5–10] and the other method is *de novo* adipogenesis, which proceeds via a two-step biological process. First, the enhanced migration of preadipocytes is accompanied by induced local neovascularization, followed by the subsequent adipogenic differentiation of preadipocytes to mature adipocytes.[11–14] Regardless of the type of approach, neovascularization appears to be essentially required to avoid necrosis and possibly to secrete unknown differentiation factors. These two different biological events of angiogenesis and adipogenesis have been proven to be promoted by the addition of basic fibroblast growth factor (bFGF) for the former process and insulin and insulin-like growth factor I (IGF-I) for the latter process.[11–16]

For example, *de novo* adipogenesis was realized by injecting a mixed solution of an extract of a basement membrane (Matrigel) and bFGF[11] or gelatin microspheres immobilized with bFGF,[12,13] or by injecting poly(lactic-co-glycolic-acid)-polyethylene glycol (PLGA/PEG) microspheres coimmobilized with insulin and IGF-I into the subcutaneous lesion.[14] However, an attempt at long-term simultaneous delivery of both angiogenic and adipogenic factors to generate adipose tissues has not yet been reported.

Our approach toward *de novo* adipose tissue formation aims at the construction of a long-term simultaneous delivery system for angiogenic (bFGF) and adipogenic (insulin and IGF-I) factors, both of which are separately immobilized in photocured, styrenated gelatin microspheres (SGMs). Our previous study showed that a photocured SG matrix can serve as a drug delivery system with the following features: (1) the desired amount of drug in a photocured matrix can be easily loaded and (2) the drug release rate can be controlled.[17]

Our strategy by which *de novo* adipose tissue formation is accelerated involves coinjection of three different types of photocured SGMs, each of which is immobilized with protein drugs of different biological activities. Because an ideal scenario of *de novo* adipogenesis involves a sequential or simultaneous process of capillary formation and accumulation and differentiation of preadipocytes to adipocytes, co-use of SGMs with the fast release characteristic of bFGF and SGMs and the relatively slow release characteristic of both insulin and IGF-1 may be beneficial. In this study, the preparation of SGMs, and their *in vitro* drug release characteristics, are described and the adipogenic effects on implantation of these microspheres into subcutaneous lesions of rats are examined.

MATERIALS AND METHODS

Materials

Gelatin (from bovine bone; MW, 9.5×10^4 g/mol) was purchased from Wako Pure Chemical Industries (Osaka, Japan). Water-soluble carboxylated camphorquinone (CQ), (1S)-7,7-dimethyl-2,3-dioxobicyclo[2.2.1]hepatane-1-carboxylic acid, was prepared according to the method described previously.[18] Rhodamine–lactalbumin, fluorescein isothiocyanate (FITC)–insulin, and 3,3-diaminobenzidine were purchased from Sigma (St. Louis, MO). Recombinant human basic fibroblast growth factor (bFGF) was purchased from R&D Systems (Minneapolis, MN). Recombinant human IGF-I was purchased from Genzyme (Cambridge, MA). Anti-human von Willebrand factor antibody and peroxidase-conjugated anti-rabbit IgG antibody were purchased from DakoCytomation (Carpinteria, CA). Cryostat specimen matrix (Tissue-Tek O.C.T. compound) was purchased from Sakura Finetek Japan (Tokyo). All other reagents were purchased from Wako Pure Chemical Industries.

Preparation of styrenated gelatin microspheres

The synthesis of photocurable, styrenated gelatins (styrene content, approximately 27.6 per gelatin molecule) and preparation of aqueous styrenated gelatin solutions were carried out according to procedures reported previously.[17] Briefly, styrenated gelatin was synthesized by condensation reaction of gelatin with 4-vinylbenzoic acid. The reaction mixture was dialyzed and then lyophilized, using a freeze-drier. One gram of aqueous styrenated gelatin solution was poured into 20 mL of liquid paraffin with 0.2% Span 85 and stirred at 120–150 rpm under visible light irradiation, using an 80-W halogen lamp (Tokusou Power Lite; Tokuyama, Tokuyama, Japan; wavelength, 400 nm $< \lambda <$ 520 nm; irradiation intensity, 1.3×10^6 lux) for 20 min. After the addition of 20 mL of hexane, the gelatin microspheres formed were collected by filtration through a glass fiber filter (pore size, 0.6 μm). The microspheres were then washed three times with 40-mL aliquots of hexane to remove residual paraffin, and dried for 1 h at room temperature. SGMs were used in further *in vitro* or *in vivo* experiments immediately after preparation.

Morphological analysis of microspheres

SGM morphology was determined by scanning electron microscopy (SEM) (JSM-6301F; UEOL, Tokyo, Japan). Particle size was determined on the basis of randomly selected 500 microspheres from 5 fields of view, using an optical microscope (TE300; Nikon, Tokyo, Japan) fitted with a micrometer scale.

In vitro *drug release*

Two hundred milligrams of aqueous gelatin solution containing 0.1 wt% CQ and 0.2 wt% rhodamine–lactalbumin or FITC–insulin as model drugs, was poured into the bottom of a well of a 48-well dish, and then irradiated with 1.3×10^6 lux of visible light for 3 min to form a gel. Disk-type gels were dispensed into a 12-well dish. Two milliliters of phosphate buffer solution (PBS, pH 7.4) supplemented with penicillin and streptomycin was added to each well and liquid samples were withdrawn from the wells at regular intervals at 37°C. The amount of model drug released from the gel was determined spectrophotometrically at 558 nm for rhodamine–lactalbumin and at 493 nm for FITC–insulin, respectively (DU 530; Beckman Coulter, Fullerton, CA).

In vivo *experiments*

Animal experiments were reviewed by the Committee on the Ethics of Animal Experiments (Faculty of Medicine, Kyushu University, Fukuoka, Japan) and carried out in accordance with the *Guidelines for Animal Experiments* of the Faculty of Medicine, Kyushu University and the law (no. 105) and notification (no. 6) of the Japanese government. Six-week-old male Wistar rats (Kyudou, Saga, Japan) were anesthetized by intraperitoneal injection of pentobarbital (40 mg/kg). Either bFGF, insulin, or IGF-I was premixed with aqueous styrenated gelatin solution, and SGMs were prepared according to the procedure described previously. The gelatin concentrations were 20% for bFGF-immobilized SGMs and 30% for insulin- or IGF-I-immobilized SGMs. One hundred milligrams of bioactive substance-immobilized SGMs was injected subcutaneously into the dorsal area bilaterally. Table 1 details the SGMs used in these experiments, with their various contents of bioactive substances. For group IV, two different SGMs, each immobilized with insulin (2 IU/100 mg of SGM) or IGF-I (2 μg/100 mg of SGM), were prepared separately, and mixed in equal amounts and injected at each site. For group V, three types of SGMs immobilized with either bFGF (3 μg/100 mg of SGM), insulin (3 IU/100 mg of SGM), or IGF-I (3 μg/100 mg of SGM) were prepared and mixed in equal amounts for injection. SGMs without any bioactive substances were used as control. The amount of immobilized insulin was determined approximately from our preliminary animal experiments. That is, a single subcutaneous injection of a quantity 10-fold higher than the total immobilized amount (10 IU of insulin for injected SGMs used for this study) in the backs of rats resulted in death within 1 day of injection, whereas injection of one-tenth the total immobilized amount resulted in no adipose tissue formation. The amount of total immobilized IGF-I was determined from those in previous papers.[14–16] Four rats for each experimental group were used and samples were harvested for further studies.

TABLE 1. EXPERIMENTAL GROUPS[a] AND INGREDIENTS FORMULATION

	Active ingredient (per 100 mg of SG)		
Group no.	*bFGF (μg)*	*Insulin (IU)*	*IGF-I (μg)*
I (0.01)	0.01	—	—
I (0.01)	0.1	—	—
I (1)	1	—	—
I (10)	10	—	—
II	—	1	—
III	—	—	1
IV	—	1	1
V	1	1	1
VI (control)	—	—	—

[a]*Group I:* SGMs immobilized with bFGF at four different concentrations (μg per 100 mg of photocured SG) (group I [0.01 μg], group I [0.1]; group I [1], and group I [10]). *Group II:* SGMs immobilized with 1 IU of insulin per 100 mg of photocured SG. *Group III:* SGMs immobilized with 1 μg of IGF-I per 100 mg of photocured SG. *Group IV:* SGMs immobilized with 1 IU of insulin and 1 μg of IGF-I per 100 mg of photocured SG. *Group V:* SGMs immobilized with 1 μg of bFGF, 1 IU of insulin, and 1 μg of IGF-I per 100 mg of photocured SG. *Group VI:* SGMs immobilized with no ingredient.

Histological studies

Skin paddles with underlying subcutaneous tissue (2×2 cm^2), including the site of injection, were harvested and fixed in 10% formalin. For groups I (0.01) (0.01 μg of bFGF per 100 mg of SGM), I (0.1), I (1), I (10), and VI, the specimens were embedded in paraffin and sectioned, followed by staining with hematoxylin and eosin (H&E) or immunostaining with an antibody to human von Willebrand factor at a dilution of 1:1600 at 4°C for 16 h. After further incubation with the peroxidase-conjugated anti-rabbit IgG antibody, peroxidase activity was visualized with 3,3-diaminobenzidine. The immunostained sections were counterstained with hematoxylin. Twenty different fields were selected from fibrous tissue surrounding residual injected SGMs for determining the number of capillaries (×200 magnification). For groups I (1), II, III, IV, V, and VI, the specimens were divided into two pieces. One-half of each specimen was embedded in paraffin for H&E and von Willebrand factor staining, and the remaining half was embedded in O.C.T. compound, cryosectioned, and stained with Sudan IV.

Lipid analysis

Fibrous tissue (2×2 cm^2), which lies in between the cutaneous muscle of the trunk and the superficial mus-

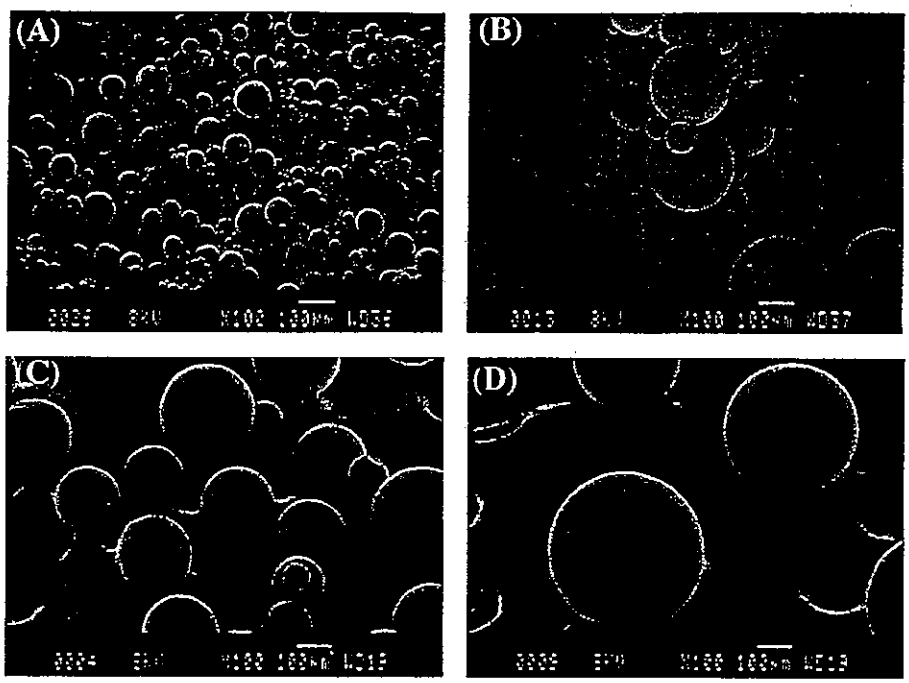

FIG. 1. Scanning electron micrographs of SGMs. SG concentration: (A) 20%, (B) 30%, (C) 40%, (D) 50%.

cles of the back, including the site of SGM injection, was harvested. The specimens were minced and homogenized in distilled water. Total lipid was extracted with chloroform–methanol (2:1, v/v) and centrifuged for 5 min at 1.2×10^4 rpm. The mixed organic solution layer containing triacylglycerol was extracted and placed under vacuum to evaporate the chloroform and methanol. Triacylglycerol content was measured with a triglyceride E-test kit (Wako Pure Chemical Industries) according to the manufacturer's instructions.

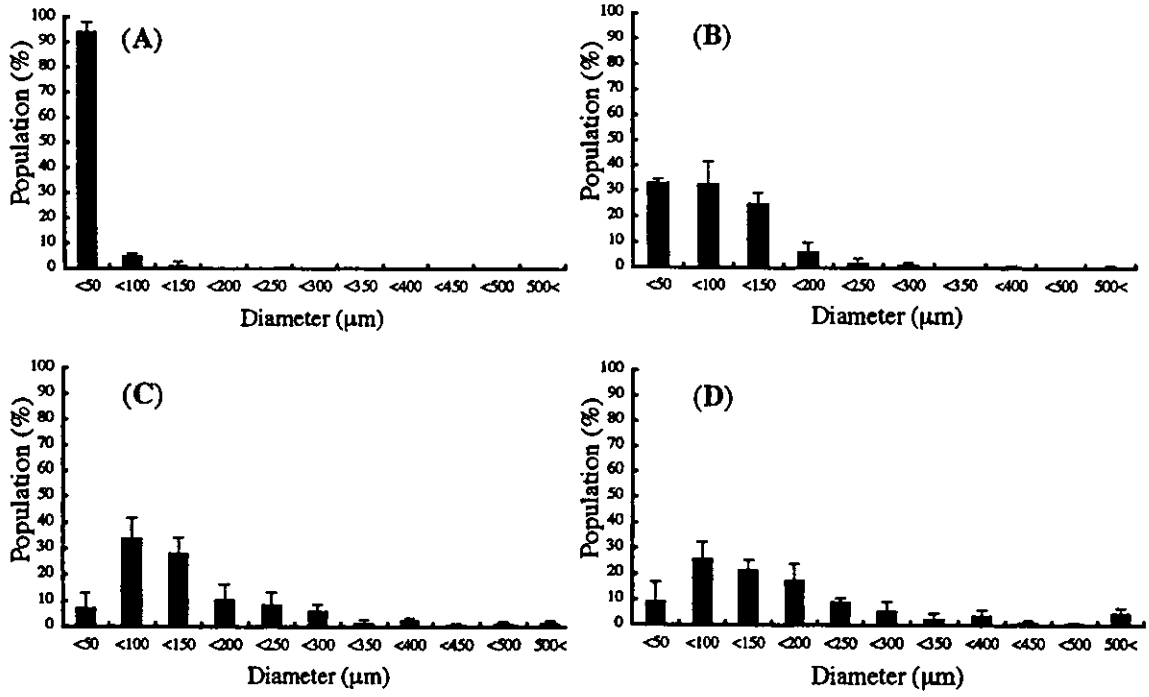

FIG. 2. Particle size distribution of SGMs. SG concentration: (A) 20%, (B) 30%, (C) 40%, (D) 50%.

TABLE 2. MEAN PARTICLE DIAMETER OF SGMs AS FUNCTION OF SG CONCENTRATION

SG concentration (wt %)	*Mean diameter (μm ± SD)*[a]
20	25.4 ± 18.6
30	85.9 ± 69.9
40	145.8 ± 113.4
50	187.1 ± 234.5

Abbreviations: SG, styrenated gelatin; SGMs, styrenated gelatin-based microspheres.

[a]The data were statistically determined on the basis of 500 particles randomly selected from 5 fields of view, using an optical microscope.

Statistical analysis

Experimental results were expressed as means ± standard deviation (SD). The data were subjected to statistical analysis (analysis of variance, ANOVA). Statistical analysis was carried out by ANOVA with a Tukey–Kramer post hoc test; $p < 0.05$ was considered statistically significant. All statistical analyses were performed with StatView 5.0 (Abacus, Berkley, Calif., USA).

RESULTS

Preparation and morphological analysis of photocured gelatin microspheres

Styrenated gelatin (SG)-based microspheres (SGMs) were prepared by dispersing an aqueous solution containing SG and carboxylated camphorquinone as a photocleavable radical generator in liquid paraffin under stirring at room temperature and subsequently subjecting it to visible light irradiation. SEM observations revealed that the SGMs obtained by filtration are fairly round particles with a smooth surface (Fig. 1A–D). Qualitatively, at higher SG concentration, larger microspheres with a broader diameter distribution were obtained. In a quantitative study to determine population size, the obtained histograms show that, at the lowest SG concentration (20%), the size of the majority of microspheres was below 50 μm, and that an increase in SG concentration resulted in a heterogeneous size distribution (Fig. 2A–D). The mean particle diameter of SGMs ranged from approximately 25 to 187 μm, depending on SG concentration (Table 2).

In vitro *drug release*

The SG concentration-dependent release characteristics of model drugs, as shown below, were determined as follows: the photocured SG disks (diameter, 12 mm; thickness, 1.8 mm) were prepared from a premixed solution of SG with a model protein, rhodamine–lactalbumin, the molecular weight of which (1.4×10^4) is almost identical to that of bFGF (1.6×10^4), and FITC–insulin, the molecular weight of which (6.1×10^3) is almost identical to those of insulin (5.7×10^3) and IGF-I (7.6×10^3), at various SG concentrations in the wells of culture dishes. The time course of the release of the model protein into a buffer solution was determined spectrophotometrically. Figure 3A and B shows the time-dependent fractional change in the amount of released rhodamine–lactalbumin and FITC–insulin from SG disks prepared at different SG concentrations, respectively. Irrespective of SG concentration, the release profiles are characterized by an initial burst of protein release during the first day, followed by prolonged release at a lower rate for up to 21 days (length of observation period). The fractional releases of both rhodamine–lactalbumin and FITC–insulin were dependent on SG concentration: the higher the SG concentration, the lower the release rate. Significant differences in release rate were not observed

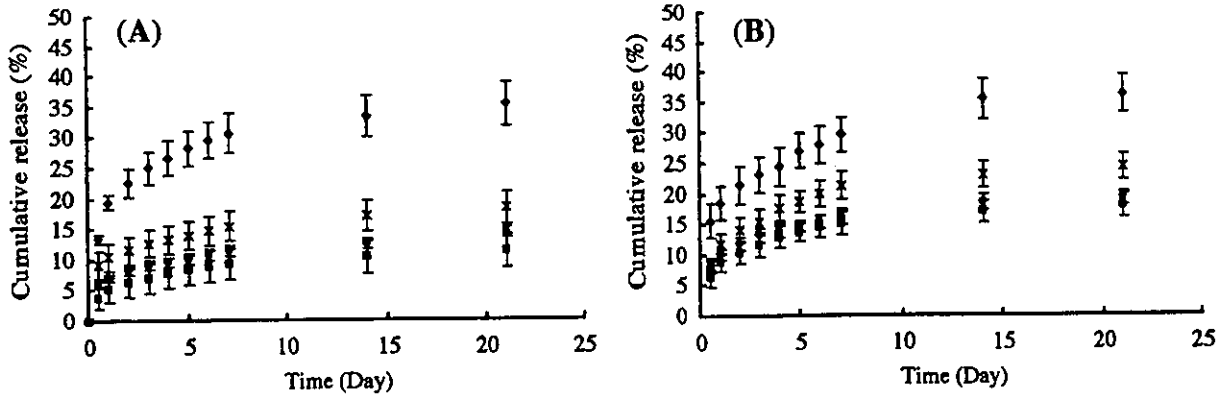

FIG. 3. Fractional release of (A) rhodamine–lactalbumin and (B) FITC–insulin from SG disks ($n = 4$). SG concentration: 20 wt% (◆), 30 wt% (×), 40 wt% (●), and 50 wt% (■). CQ concentration: 0.1 wt% of SG. Visible light irradiation: 3 min at a photointensity of 1.3×10^6 lux. Values are expressed as means ± SD.

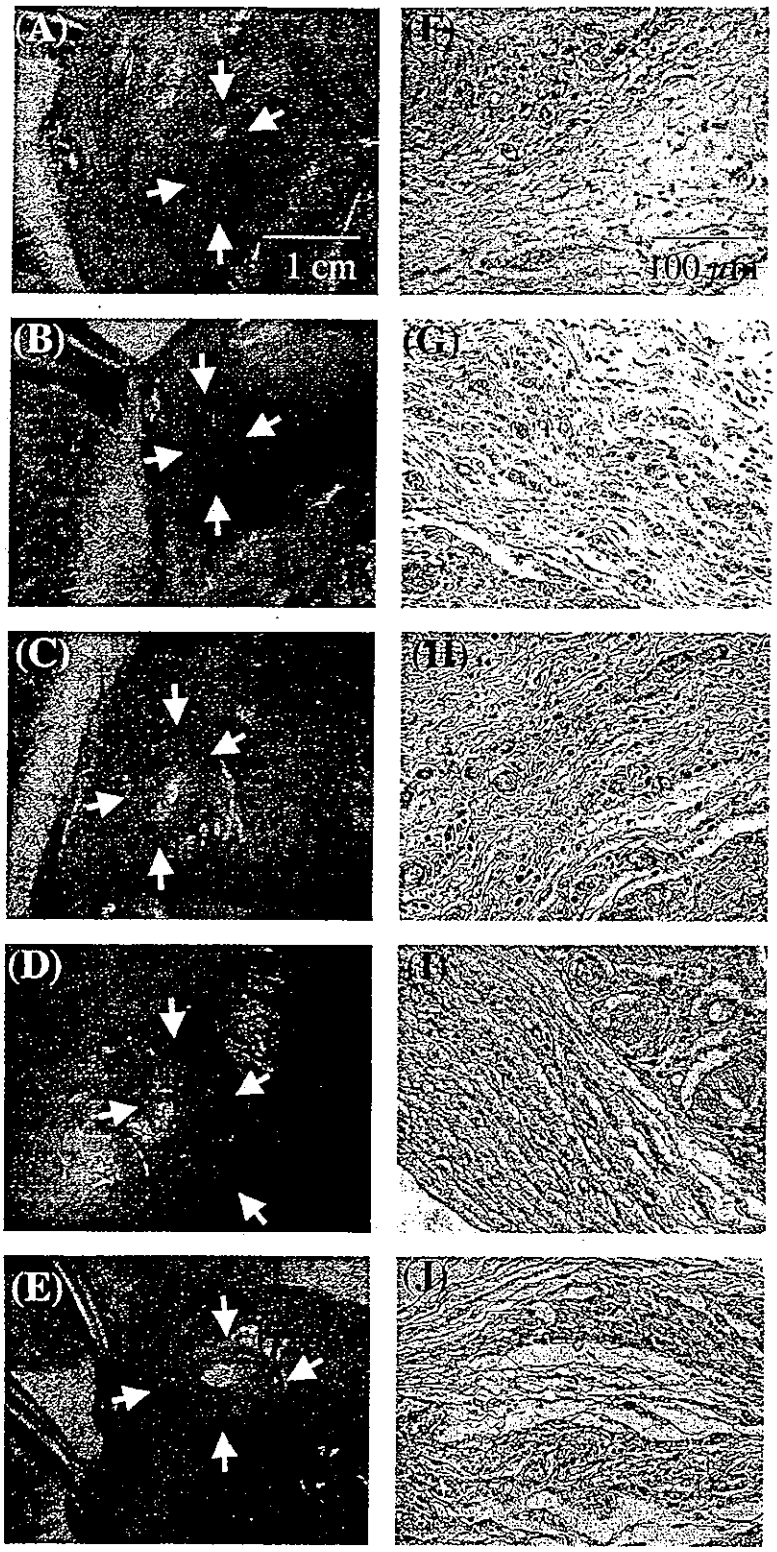

FIG. 4. Tissue appearance (A–E, surrounded by arrows) and von Willebrand factor-staining sections (F–J) of injection site, 2 weeks after injection of SGMs immobilized with 0.01 [A and F: group I (0.01)], 0.1 [B and G: group I (0.1)], 1 [C and H: group I (1)], 10 [D and I: group I (10)], and 0 (E and J: group VI) μg of bFGF.